Computational Investigation of Melt Pool Process Dynamics and Pore Formation in Laser Powder Bed Fusion

Bo Cheng, Lukas Loeber, Hannes Willeck, Udo Hartel, and Charles Tuffile

In the laser powder bed fusion additive manufacturing process, the presence of porosity may result in cracks and significantly affects the part performance. A comprehensive understanding of the melt pool process dynamics and porosity evolution can help to improve build quality. In this study, a novel multi-physics computational fluid dynamics (CFD) model has been applied to investigate the fluid dynamics in melt pools and resultant pore defects. To accurately capture the melting and solidification process, major process physics, such as the surface tension, evaporation as well as laser multi-reflection, have been considered in the model. A discrete element method is utilized to model the generation of powder spreading upon build plate by additional numerical simulations. Multiple single track experiments have been performed to obtain the melt pool shape and cross-sectional dimension information. The predicted melt pool dimensions were found to have a reasonable agreement with experimental measurements, e.g., the errors are in the range of 1.3 to 10.6% for melt pool width, while they are between 1.4 and 15.9% for melt depth. Pores are captured by both CFD simulation and x-ray computed tomography measurement for the case with a laser power of 350 W and laser speed of 100 mm/s. The formation of keyholes maybe related to the melt pool front wall angle, and it is found that the front wall angle increases with the increase in laser line energy density. In addition, a larger laser power or smaller scanning speed can help to generate keyhole-induced pores; they also contribute to produce larger sized pores.

1. Introduction

In the powder bed fusion additive manufacturing process, the presence of pores can lead to cracks and significantly affect the fatigue strength of fabricated parts (Ref 1). In the laser powder bed fusion (L-PBF) process, where a high-energy laser beam is utilized to selectively scan thin slices of 2D cross sections of an engineering component, the generation of defects such as porosity is inevitable due to locally rapid heating and cooling. Therefore, there is an urgent need for a fundamental understanding of the pore formation since different physical mechanisms may lead to different types of porosity, e.g., lack of fusion-induced pores and keyhole-induced pores. Lack of fusion-induced pores is likely to be formed if a low energy beam irradiates the top powder layer since the powder particles may not be fully melted and pores between particles remain unfilled by molten metal fluid. On the contrary, keyhole-induced pores may be generated if excessive energy is applied on the powder bed, where the melt pool as well as keyhole

dynamics can contribute to the formation of pores beneath the powder bed. Figure 1 shows the schematic plot of the general phenomena in the L-PBF, which is also called selective laser melting (SLM).

The effect of process parameters on porosity evolution in AlSi10 Mg samples was experimentally investigated by Aboulkhair et al. (Ref 2). Fabricated samples were cross-sectioned and polished to study the presence of pores using optical microscopy, and the process window for high density (low porosity) parts was presented. In addition, Gong et al. (Ref 3) performed indirect measurements of melt pool cross sections after solidification. They conducted multiple sets of single track experiment with different laser speeds and powers, and the melt pool as well as pore characteristics were investigated to identify the pore-related laser process parameters. Computed tomography (CT) is another method to analyze the porosity in solidified material. Siddique et al. (Ref 4) were able to detect pore defects using CT in L-PBF parts, and they studied the built part quality and pore characteristics. The results showed that the pores close to the surface had a higher stress concentration factor. In addition, the samples with pores had more fatigue scatter when compared with samples without pores. Cai et al. (Ref 5) applied the x-ray CT method to characterize the internal pore features of L-PBF AlSi10 Mg parts. Their CT results illustrated that increasing the laser power could help to reduce or eliminate the material porosity level. Furthermore, the sample density measured by Archimedes method agreed well with the CT measurement. Shrestha et al. (Ref 6) conducted single track experiments using Ti-6Al-4V powder with different laser powers and speeds; additionally, micro-CT was used to analyze the number and volume of pores. It was found that the change of laser power had a larger influence on pore formation than

Bo Cheng and **Charles Tuffile**, Robert Bosch LLC, Research and Technology Center, Cambridge, MA 02139; and **Lukas Loeber, Hannes Willeck,** and **Udo Hartel**, Robert Bosch GmbH, Renningen 71272, Germany. Contact e-mail: bo.cheng@us.bosch.com.
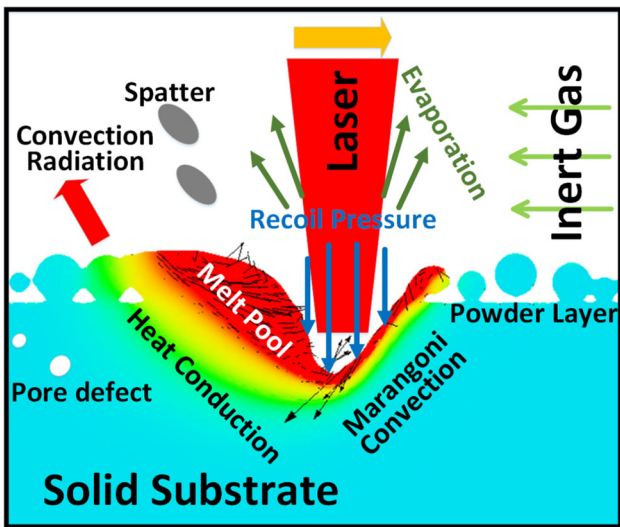
Fig. 1 Schematic plot of the general phenomena in the L-PBF additive manufacturing process

laser speed under the same laser energy density. The overall pore volume increased when the laser power changed from 20 to 140 W; however, the pore volume decreased when laser power increased beyond 140 W. In situ direct measurement of defect generation in the L-PBF processes, such as keyhole-induced pore formation is challenging due to short time and small domain of their occurrence. With the help of synchrotron x-ray imaging system, Leung et al. (Ref 7) investigated the physical mechanisms of laser–material interactions and powder consolidation in the L-PBF process, including the formation of porosity and spatter. They showed that the metal fluid flow was dominated by the Marangoni convection effect. The pore history was captured, including formation, motion, dissolution and dispersion in the melt zone. The generation of spatters from the melt pool was observed as well. Recently, Cunningham et al. (Ref 8) made a major breakthrough for the direct observation of melt pool evolution in L-PBF. Utilizing the ultrahigh-speed synchrotron x-ray imaging technique, they visualized the development of keyholes in the laser melting process. With the help of high spatial (ca. 2 μm) and temporal (in the range of 50 to 400 kHz) resolutions provided by the x-ray synchrotron facility, they demonstrated that the geometry of the vapor caused melt pool recession varies in a systematic fashion. The unstable keyholes were observed to be formed at high laser power and low laser velocity, where pores can be generated if the keyhole aspect ratio is too high.

On the other hand, physics-based numerical models can help to predict the critical process physics in L-PBF, such as melt pool flow, material evaporation and keyhole formation. To capture the lack of fusion porosity in the L-PBF multilayer powder deposition process, a two-layer microscale thermo-fluid model was developed by Shrestha and Chou (Ref 9). The deposition of powder particles was simulated by dropping spheres according to encountered trajectory of obstacles or solidified surfaces. They demonstrated that inter-layer porosity, due to insufficient melting between different layers, could be formed at high laser scanning speed. By introducing the randomly distributed powder bed and thermo-fluid properties

into a transient finite volume method (FVM) model, Xia et al. (Ref 10) simulated the pores on the solidified top powder layer as well as the pores between different layers. Yan et al. (Ref 11) proposed a powder scale FVM model to predict the build defects in powder bed electron beam selective melting (EBSM). They showed that potential porosity could be generated between different solidified tracks in the same layer if the hatch spacing was not appropriately decided. The formation of keyhole-induced pores has also been simulated in the L-PBF process; Tan et al. (Ref 12) investigated the laser input energy density effect on porosity generation in the single track scanning process using an experimentally verified computational fluid dynamics (CFD) model. They found that the collapse of deep keyholes, generated by high laser power or low laser speed, could cause porosity formation beneath the powder layer. To have a comprehensive understanding of pore formation in the L-PBF process, the accurate modeling of bubble formation and its evolution to porosity are necessary. In the keyhole laser melting process, multi-reflections of the laser rays in the keyhole can affect the overall energy absorption in the melt pool and may lead to a sharper and deeper keyhole, resulting in pore defects. However, simulation works considering bubble generation, laser multi-reflection in keyholes and pore defect formation for L-PBF process have rarely been provided.

A high-fidelity thermo-fluid L-PBF additive manufacturing model can provide comprehensive information for the dynamics of melt pools and keyholes, as well as pore characteristics. This paper aims to develop a novel powder-scale CFD model to study the fluid flow of melt pools and evolution of pores with the consideration of a laser multi-reflections feature in the keyhole. The powder distribution upon a solid substrate was simulated by the discrete element method (DEM) model. In addition, a multi-physics single track CFD model was utilized to investigate the formation of keyhole-induced pores. The numerical model was validated against experimentally obtained melt pool cross-sectional images.

2. Modeling Approach

2.1 Powder Bed Generation

To accurately model the generation of one powder layer upon a solid substrate, a DEM model was applied to simulate the movement of powder particles. In the DEM model, the particles are assumed to be perfect spheres with different diameters. The interaction forces can be obtained by calculating particle to particle contacting force and gravitational force. The particle motion has been solved using Newton's second law of motion. The powder size (diameter) distribution used was from experimental measurement of L-PBF powders. To simulate the creation of the powder bed, a moving blade was utilized to spread one layer of powder particles with a given layer thickness after a cloud of powder particles was freely dropped upon the powder container. The detailed DEM modeling process can be found in (Ref 13, 14). The geometrical information of the powder layer will then be used for the melt pool dynamics simulation. Figure 2 shows the exemplary plot of the generation of one layer of powder.
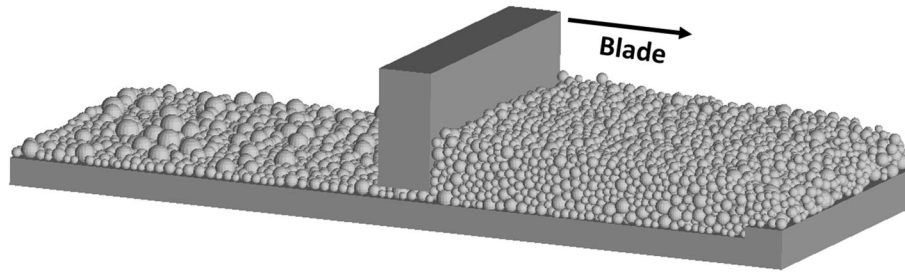
Fig. 2 Exemplary plot of powder bed generation with different sized particles

2.2 Thermo-Fluid Simulation

2.2.1 Thermal and Fluid Flow Simulation Mathematical Model. A microscale multi-physics CFD finite volume method (FVM) model was applied using the commercial software FLOW3D® to study the melt pool characteristics. The melted material was assumed to be incompressible, laminar and Newtonian. FLOW3D® software numerically solved the conservation equations of mass, momentum and energy (Ref 13):

Mass:

$$\nabla \cdot \vec{v} = 0 \tag{Eq 1}$$

Momentum:

$$\frac{\partial \vec{v}}{\partial t} + (\vec{v} \cdot \nabla)\vec{v} = -\frac{1}{\rho}\nabla P + \mu \nabla^2 \vec{v} + \vec{g} + F_b \tag{Eq 2}$$

Energy:

$$\frac{\partial h}{\partial t} + (\vec{v} \cdot \nabla)h = -\frac{1}{\rho}(\nabla \cdot k\nabla T) + \dot{q} \tag{Eq 3}$$

where $\vec{v}$ is the molten fluid velocity, t is the time, P is the pressure, ρ is the material density, μ is the fluid viscosity, $\vec{g}$ is the gravitational acceleration, F_b is the body force in the system, h is the enthalpy, k is the conductivity, and T is the temperature, $\dot{q}$ is the external heat source.

The volume of fluid (VOF) method was utilized to reconstruct the free surface evolution when powder particles are heated and melted by the high-energy laser beam. The fluid volume fraction in one cell, F, is set to be between 0 and 1. $F = 1$ means the cell is filled with fluid while $F = 0$ indicates the cell is empty. The equation is shown below:

$$\frac{\partial F}{\partial t} + \nabla \cdot (\vec{v}F) = 0 \tag{Eq 4}$$

The surface tension caused Marangoni effect may significantly affect the flow behavior in the melt pool. Therefore, the following equation is used to describe the change of surface tension against temperature:

$$\sigma(T) = \sigma_0 + \frac{d\sigma}{dT}(T - T_L) \tag{Eq 5}$$

where σ_0 is the surface tension at liquidus (melting) temperature (T_L), and $d\sigma/dT$ is the surface tension gradient.

Due to high-energy input, the material will undergo phase transformations, such as solid to liquid and liquid to vapor. The latent heat of fusion effect is considered in the model to
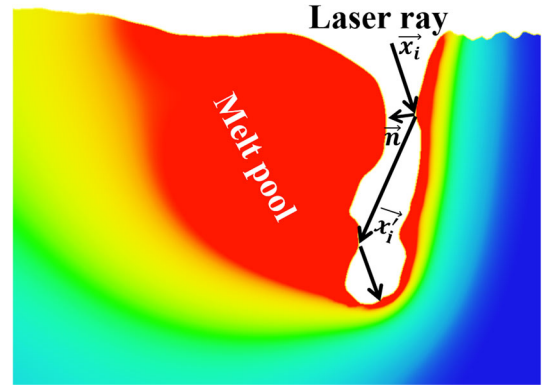

Fig. 3 Schematic plot of laser multiple reflection inside keyhole

describe the solid to liquid state change. It is calculated as an additional thermal energy term based on liquid fraction (per unit mass). In addition, the temperature within or around the laser center region may exceed the material boiling temperature. The loss of evaporated material (liquid to metal vapor state change) can carry away a significant amount of energy. The evaporation caused heat loss can be calculated as (Ref 13):

$$Q_{vapor} = \frac{0.82\Delta h_v}{\sqrt{2\pi MRT}} P_0 \exp\left(\Delta h_v \frac{T - T_{boil}}{RTT_{boil}}\right) \tag{Eq 6}$$

where Δh_v is the enthalpy of metal vapor (latent heat of vaporization), M is the molar mass, P_0 is the atmospheric pressure, R is the universal gas constant, and T_{boil} is the boiling temperature.

In addition, the evaporated metal can cause a pressure upon the melt pool surface, which is known as recoil pressure (P_{recoil}). The recoil pressure is modeled as (Ref 13, 15):

$$P_{recoil} = 0.54P_0 \exp\left(\Delta h_v \frac{T - T_{boil}}{RTT_{boil}}\right) \tag{Eq 7}$$

Laser multiple reflection can happen in keyholes, as shown in Fig. 3. The laser ray will go through several reflections by the keyhole wall and complicate the distribution of laser energy. Therefore, a ray tracing technique is employed to incorporate the multiple laser reflection phenomena into keyholes (Ref 16). The reflected laser ray can be calculated as follows:

$$\vec{x_i'} = \vec{x_i} - 2(\vec{x_i} \cdot \vec{n}) \tag{Eq 8}$$

where $\overrightarrow{x_i'}$ is the reflected laser vector, $\overrightarrow{x_i}$ is the incoming laser vector which irradiates the free surface of keyhole, and $\vec{n}$ is the surface normal.

2.2.2 Laser Heat Source Modeling. The laser energy distribution was assumed to be a moving surface heat flux with a Gaussian distribution, as shown below:

$$Q = \frac{\eta P_{\text{Laser}}}{\pi R_s} \exp\left(-\frac{(x-x_s)^2+(y-y_s)^2}{R_s^2}\right) \quad \text{(Eq 9)}$$

Where η is the energy absorption coefficient, P_{Laser} is the laser power, R_s is the laser radius, and x_S and y_S are the coordinates of the laser beam center.

2.2.3 Numerical Model. To study the heat transfer, fluid flow and pore defect evolution in melt pools, a 3D microscale CFD model has been applied using the commercial software FLOW3D®. The laser beam is applied upon the top surface of powder bed and moves along the x-axis with predefined scanning speed. One layer of powder particles above the solid substrate, with geometrical information from the DEM simulation, was used to represent the newly deposited powder layer. A deep keyhole was expected in this study to allow the generation of pores; thus, a large computational domain was considered. On the other hand, only a half region was modeled for the single track laser scanning simulation so as to reduce computational cost. Therefore, the symmetric boundary condition was applied for the center plane. The numerical model had a domain dimension of $2 \times 0.35 \times 1.6$ mm ($x \times y \times z$). A uniform mesh size of 5 µm was applied to the whole computational domain, which resulted in ~ 9 million cells. The region above the powder layer was defined as void space, which has atmospheric pressure and room temperature. A preheating temperature will be applied to the whole model to represent the substrate preheating process. Figure 4 shows the configuration of the thermo-fluid model.

Type 316L stainless steel was used in this study, and its temperature-dependent thermal properties, such as conductiv-
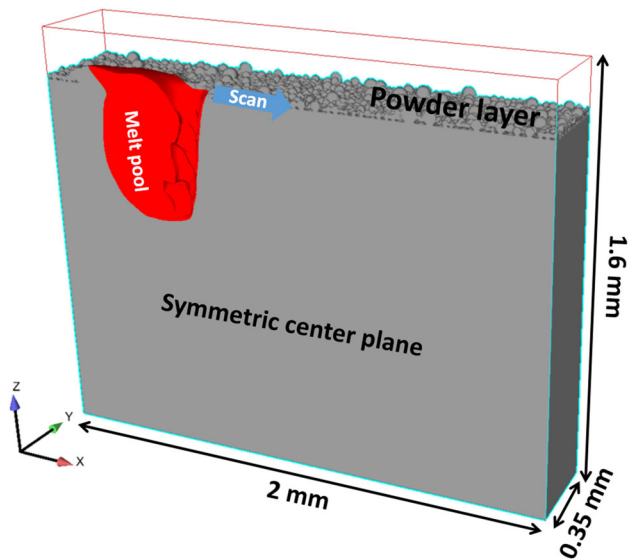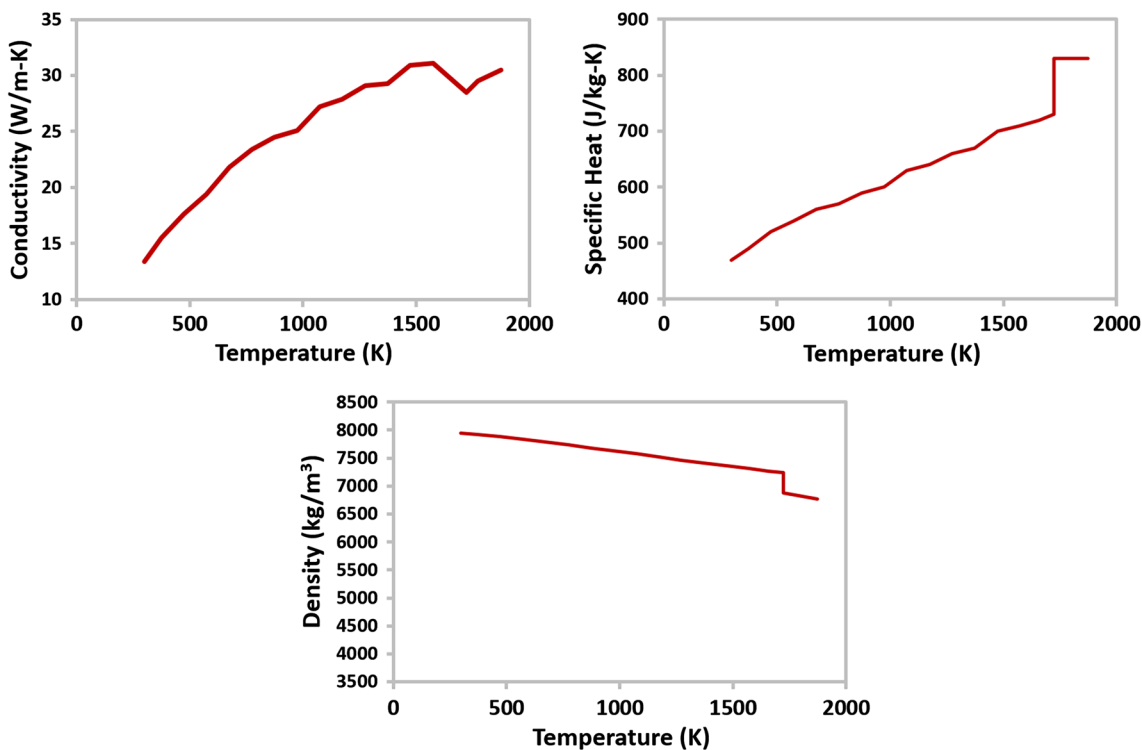
Fig. 4 Configuration of the thermo-fluid model

Fig. 5 Thermal properties of stainless steel 316L according to/taken from Ref 17

**Table 1 Thermo-physical property for stainless steel 316L**

Property	Value	References
Latent heat of fusion (L_f), kJ $\times$ kg^{-1}	270	18
Latent heat of evaporation (Δh_v), kJ $\times$ kg^{-1}	745	18
Viscosity (μ), kg $\times$ m^{-1} s^{-1}	0.008 (at 1723 K), 0.007 (at 1773 K)	17
Surface tension (σ_0), kg $\times$ s^{-2}	1.6	12
Surface tension coefficient ($\frac{d\sigma}{dT}$), kg $\times$ s^{-2} K^{-1}	−0.0008	12
Liquidus temperature (T_L), K	1723	12
Solidus temperature (T_s), K	1658	12
Boiling temperature (T_{boil}), K	3090	12
Molar mass (M), kg $\times$ mol^{-1}	0.05593	12
Laser absorption rate (η)	0.63	19
Atmospheric pressure (P_o), kN $\times$ m^{-2}	101	
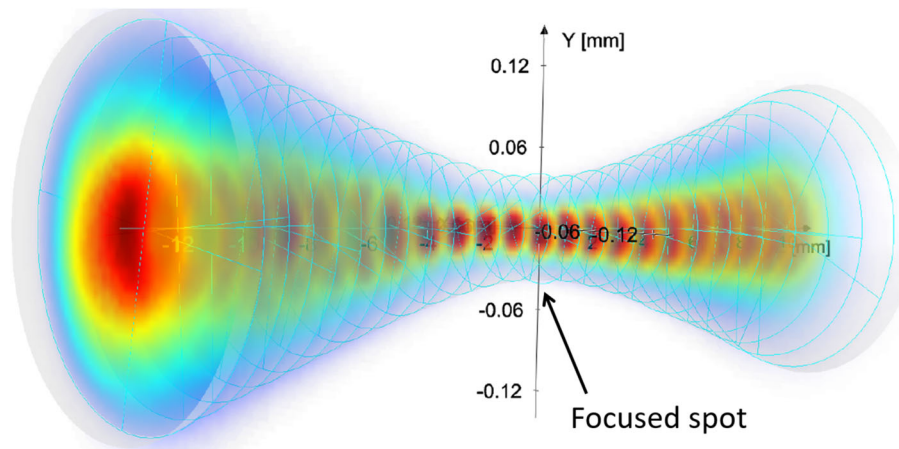
Fig. 6 Laser focus diameter used in experiment

ity, specific heat and density, are taken from the literature (Ref 17) and summarized in Fig. 5. Other thermo-physical parameters (Ref 12, 17, 18, 19), e.g., latent heat of fusion and surface tension, are listed in Table 1.

3. Experimental Details

Single track laser scanning experiments have been conducted. The heat source was a CW fiber laser with a wavelength of 1070 nm. The focused laser spot size was around 78 μm, as shown in Fig. 6. The stainless steel 316L powder material was used in this study. The powder particles had a size (diameter) distribution between 18.77 μm (D10) and 60.30 μm (D90) with a mean diameter of 36.71 μm. The particle size distribution (PSD) is summarized in Fig. 7. One layer of powder, with a thickness of ∼ 30 μm, was deposited upon a 316L stainless steel substrate. The substrate was preheated to have a uniform temperature before the single track scanning experiments. To measure the substrate temperature, five thermocouples were
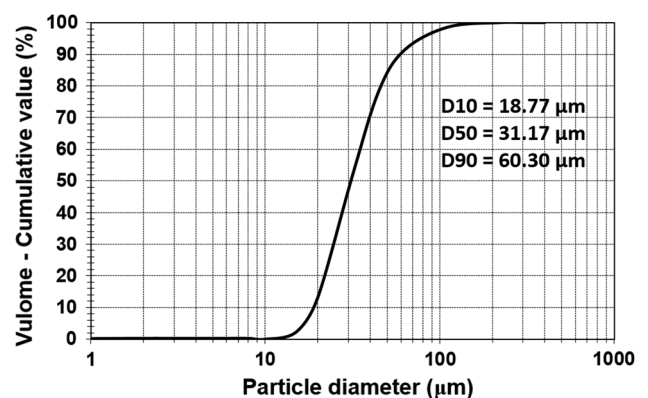
Fig. 7 Stainless Steel 316L powder cumulative PSD (diameter: μm)

placed at different locations of the substrate bottom, as shown in Fig. 8(a). A uniform substrate temperature of 150-160°C, measured on all five thermocouples, had been reached before
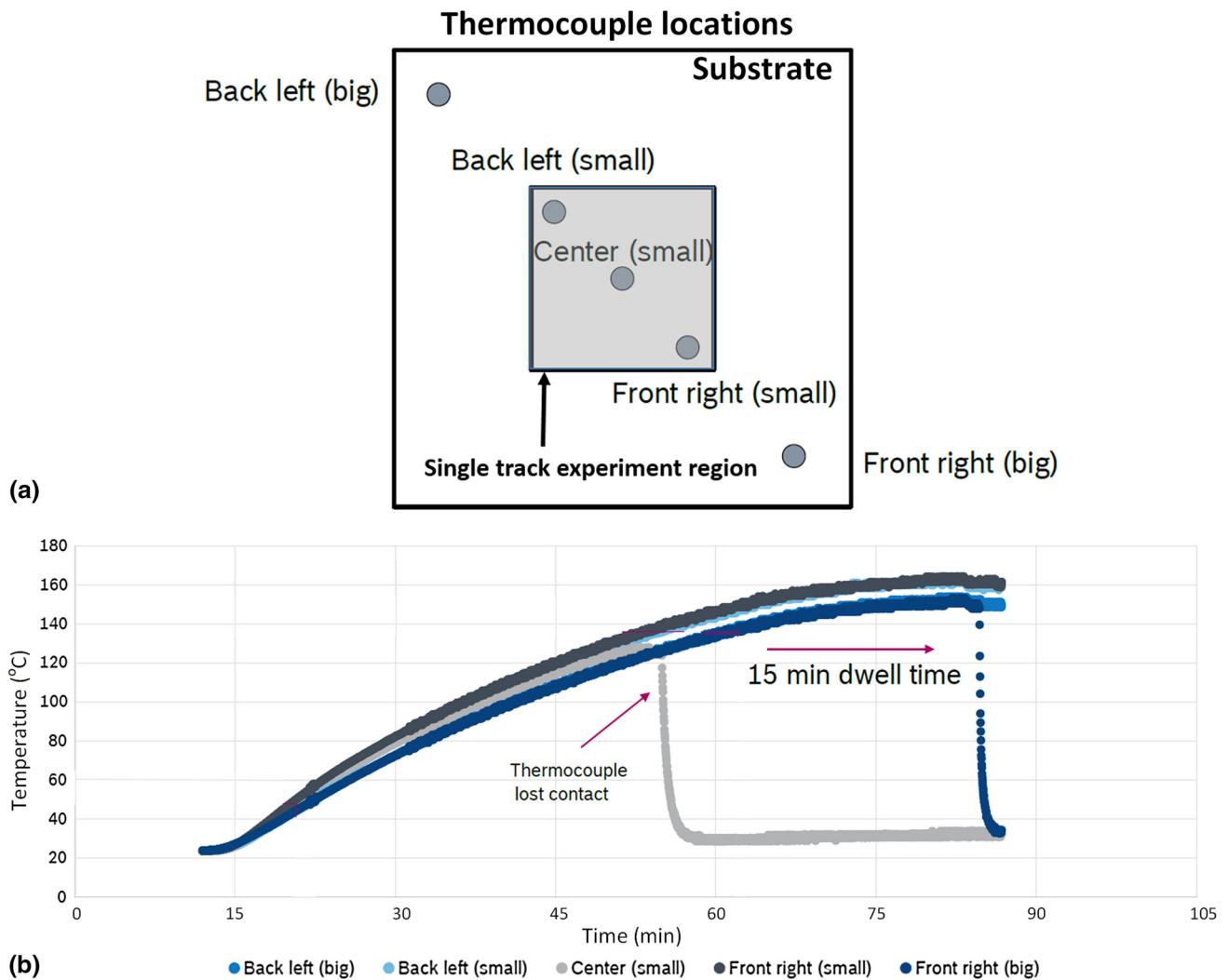
Fig. 8 Temperature measurements on substrate plate before laser scanning: (a) Location of five thermocouples on substrate; (b) Temperature vs time

laser scanning, as shown in Fig. 8(b). In order to study the process parameters effect on the melt pool characteristics, single tracks were fabricated using different laser powers and speeds. Specifically, two laser powers were used, 175 W and 350 W, and four different laser scanning speeds were tested for each laser power, namely scanning speeds of 100, 300, 500 and 750 mm/s.

4. Model Validation

All single tracks were sectioned, polished and etched for metallography to show the melt pool morphology. Figure 9 shows cross sections of single tracks (powder layer removed due to preparation) created by different combinations of laser power and scan speed. It can be seen that significantly different melt pool profiles can be created, e.g., a shallow oval shaped

melt pool is produced by 175 W laser power and 750 mm/s speed, while a deep nail shaped melt pool is generated by 350 W power and 100 mm/s speed.

To validate the numerical model developed in this work, the single track laser scanning simulations have been performed by incorporating the experimental process parameters. The powder layer was generated using the DEM model developed in section 2.1 and the experimental powder size distributions in Fig. 7. A comparison of the melt pool dimensions was conducted between simulations and experiments. Figure 9(a) and (b) compares the simulated melt zone and the experimental melt pool from different process parameters. The dimensions of melt pool depth are overpredicted; it may be due to the high absorption rate inside the keyhole introduced by laser multi-reflection model. The model prediction error is summarized in Fig. 10. It can be observed that the prediction error for melt pool width ranges from 1.3 to 10.6%, while the prediction error for melt pool depth ranges from 1.4 to 15.9%. The simulated

melt pool dimensions, from various process parameters, are in reasonable agreement with the experiments. Therefore, the developed numerical model can be used to predict the melt pool boundaries and characteristics during the laser scanning process.

Fig. 9 A comparison of experimental measurements and simulated melt pools

5. Results and Discussion

5.1 Conduction Mode Melting Simulation

Figure 11 shows the temperature distribution and melt pool characteristics of a typical case for the conduction laser melting mode. The simulation case has a laser power of 175 W and a scanning speed of 750 mm/s. Figure 11(a) presents the surface morphology and temperature of the scanning track. It can be observed that a comparatively smooth and continuous track is formed due to the melting and solidification of powder particles. During the laser melting process, the material evaporation effect will be triggered once the cell temperature reaches the boiling point of 316L steel at $T = 3090$ K. A recessed zone appears around the beam center region, which was caused by a combined effect of the melt flow and recoil pressure. The simulated results show that the maximum temperature (ca. 3300 K) at the laser beam center exceeded the evaporation point. Therefore, the energy loss due to material evaporation was calculated, e.g., heat loss from material liquid to vapor state transformation. Meanwhile, the vapor-induced recoil pressure applied on the free surface of the melt pool contributed to producing a recessed melt pool. A strong backward flow can be observed in the rear part of melt pool, as shown in Fig. 11(b). The molten material was pushed away from the higher temperature region to the lower temperature region by the surface tension force. In addition, the motion of melt flow can also be toward the recessed zone, resulting in replenishing of the recessed melt pool once the laser beam center moves away. The shape of melt pool recessed zone was found to be stable, and no abrupt collapse of the melt pool was observed during the laser scanning process, as shown in Fig. 11(c). Thus, porosity due to the dynamic of the moving melt pool is unlikely to be formed during conduction laser melting mode, e.g., no deep keyhole can be formed during this melting condition.

A surface hump may develop during the laser scanning process, as shown in Fig. 12. The surface hump is caused by backward melt flow where the molten material solidifies under the melt pool rear region. As the laser beam moves away, the
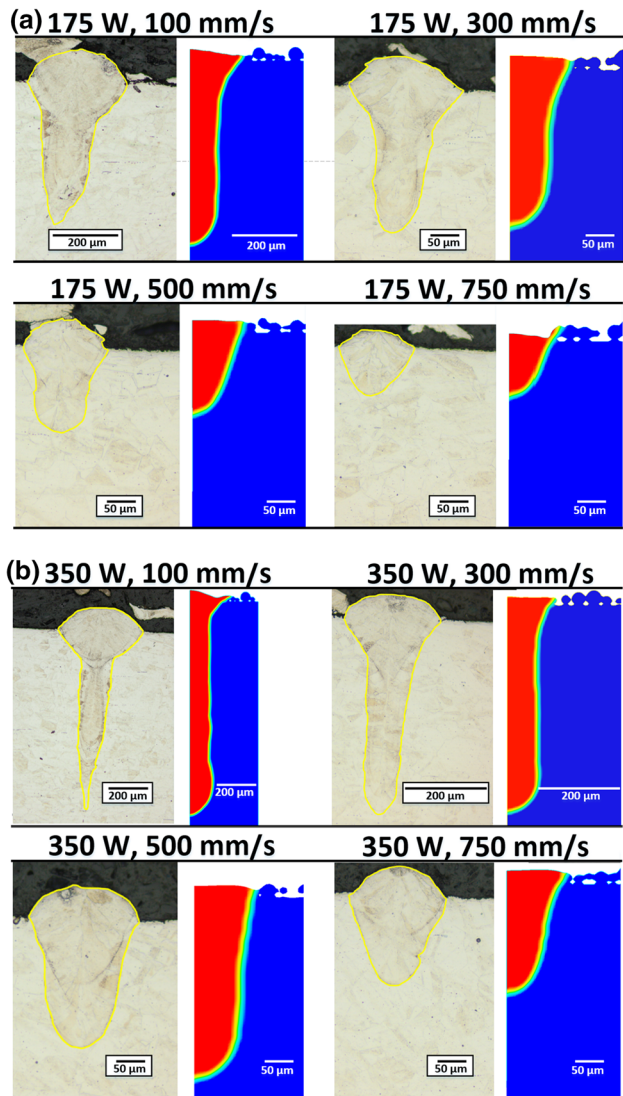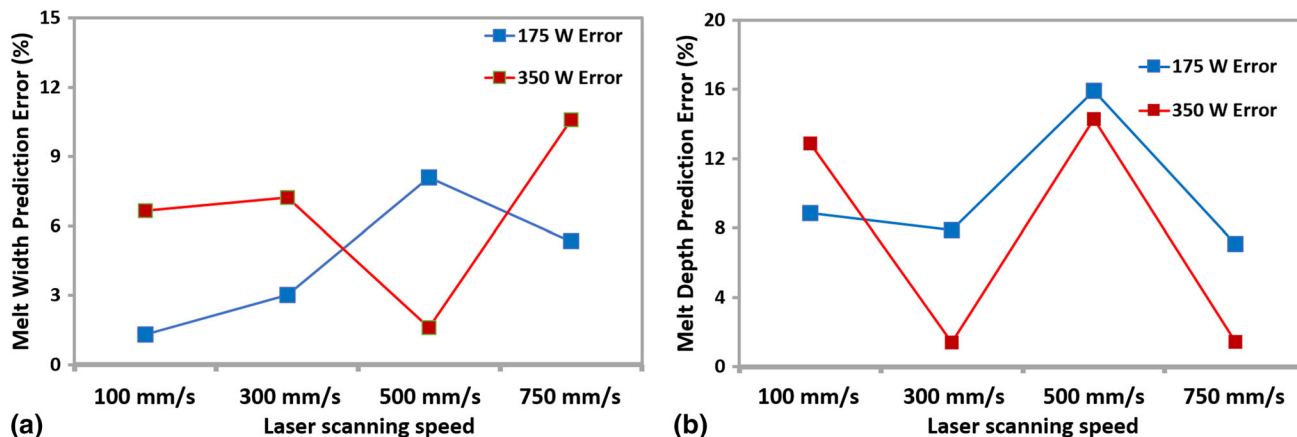

Fig. 10 Model prediction error for melt pool width and depth: (a) Prediction error for melt pool width; (b) Prediction error for melt pool depth
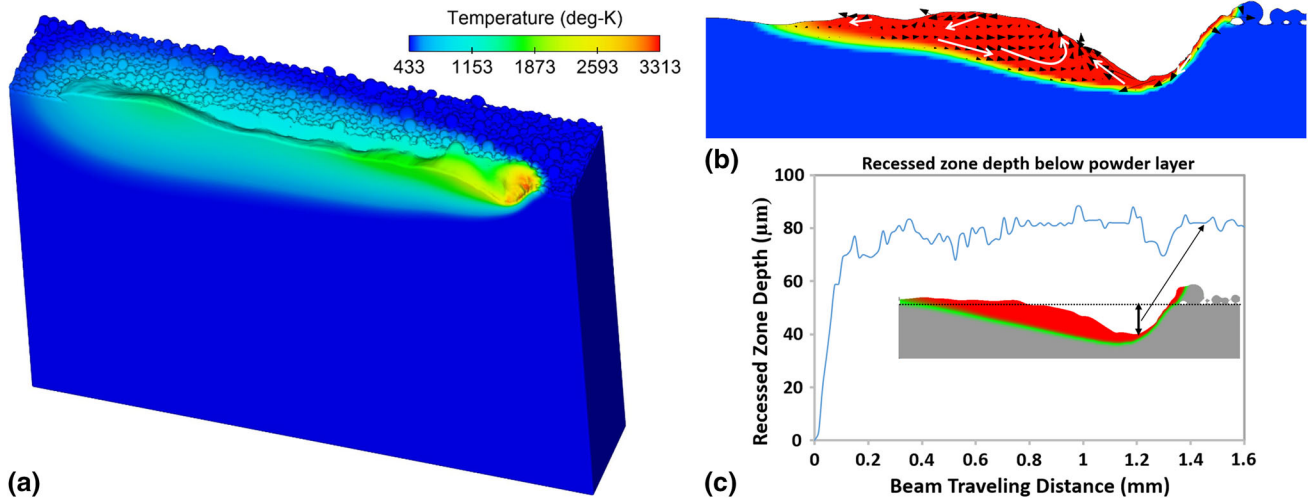
Fig. 11 Typical simulation results for conduction mode melting: (a) Temperature distribution along scanning direction; (b) Melt pool fluid flow (arrows indicating flow direction); (c) Melt pool recessed zone depth (below powder layer) against beam traveling distance, red zone indicating melt pool
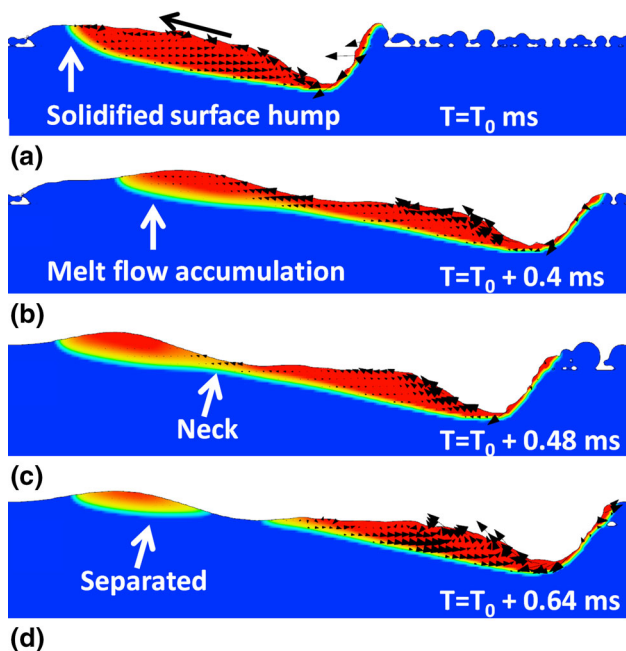

Fig. 12 Surface hump formation process

melt flow continues to accumulate above the solidified hump and increases the height of the hump that forms. As the laser beam moves further away, a narrow "melt neck" is shown between the melt pool recessed region and rear part. A separated melt zone eventually forms upon the surface hump. Meanwhile, the length of the main melt pool around the beam center reduces. The Plateau–Rayleigh instability of liquid cylinders may be used to explain the melt pool "break" phenomena: a liquid cylinder cannot maintain steady state against axial harmonic disturbances if its circumference is

smaller than the wavelength (Ref 20). In the experimental study conducted by Yadroitsev et al. (Ref 21), the authors demonstrated that the solidified melt track could form a cylindrical shape due to significant surface tension effect in L-PBF. A narrow and elongated melt pool can be unstable and break into separated droplets; thus, surface humps or even the balling effect may be generated. Another solidified surface hump may appear if the described phenomena start again.

5.2 Keyhole Mode Melting Simulation

A deep keyhole is formed when a certain threshold value for the laser intensity is reached, and thus a high amount of laser energy is applied on the scanning track. Figure 13(a) shows that a deep keyhole was formed under a laser power of 350 W and a scanning speed of 100 mm/s, e.g., melt pool depth/width = 2.8. Different sized pores, caused by the deep and unstable keyhole, can also been observed along the scanning path beneath the solidified surface. X-ray computed tomography (CT) is used to obtain pore information from experimental single track scanning samples with a predefined voxel size (geometric resolution) of 10 μm. The small sized pores in the sample, e.g., diameter < 10-20 um, may not be captured under given CT resolution. It is found that various sized pores have been generated along the scanning track at the given laser process parameters. The pores produced by the numerical model can be qualitatively compared to the experimental ones, using CT. Typical deep keyhole evolution is shown in Fig. 13(b). A shallow keyhole was formed at the early stage of laser melting. As the laser beam progressed, a deeper and irregular shaped keyhole was generated due to strong recoil pressure, Marangoni flow and evaporation effect. The surface tension causes material flow toward the void region of the keyhole, thus introducing humps along the keyhole wall. The keyhole wall may be irradiated directly by the laser beam, and it can be also irradiated by reflected laser rays, as shown in
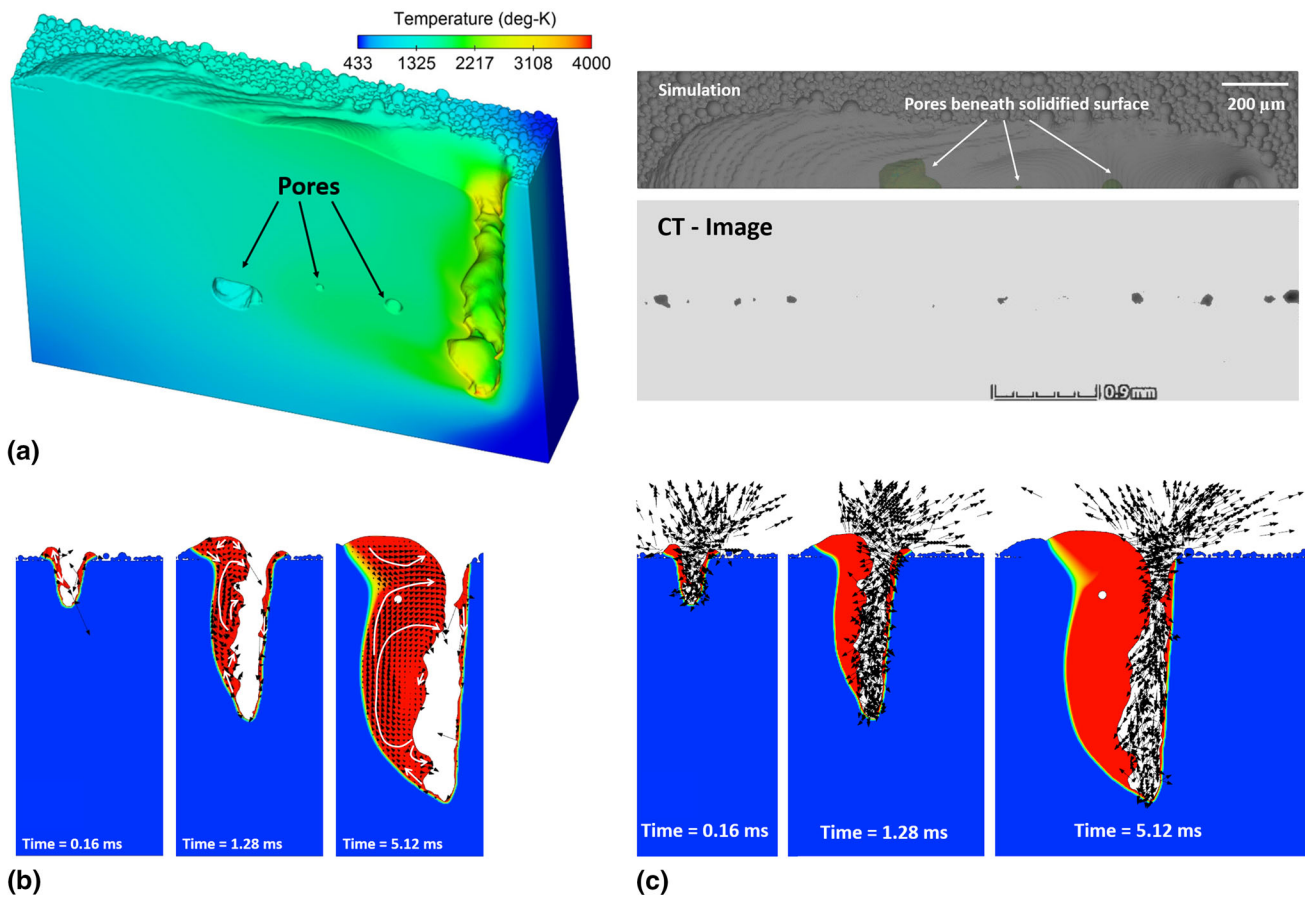
Fig. 13 Typical simulation results for keyhole mode melting: (a) Simulated and experimental pore distribution; (b) Keyhole evolution, red zone indicating melted material; (c) Laser multiple reflection in keyhole (arrows indicating reflected laser rays)

Fig. 13(c). The absorbed energy is not evenly distributed on the surface of keyhole due to the complex keyhole profile. Therefore, surface tension force may be irregularly generated because of non-uniformly distributed energy at the keyhole wall, causing oscillation of the keyhole.

The fluid flow of molten material significantly influences the keyhole stability and the pore generation. Figure 14(a) shows the collapse of keyhole and formation of a bubble. It can be seen that the molten material flows toward the keyhole void region since a strong clockwise flow is formed in the rear part of the melt pool. Humps are also generated at the rear keyhole wall; they will continue to flow toward the front wall of the keyhole. When a rear wall hump touches the front wall, the keyhole collapses and a gas bubble is generated. The newly formed bubble follows the strong vortex flow and moves away from the keyhole. However, the intense recoil pressure can reopen the enclosed bubble. Thus, not every bubble created by a keyhole leads to a pore defect. Only the bubbles that are captured by the melt pool solidification front will remain as trapped void space after the laser beam moves away. In addition, irregular pores may also be formed due to the "drag" by solidification front line, as shown in Fig. 14(b).

The large fluctuation of keyhole depth along the scanning track, due to collapsing keyholes, is observed in Fig. 15(a). The frequent collapse of keyholes can lead to intensive bubble formation in the melt pool. In addition, the change of keyhole depth may also contribute to the formation of irregular spikes at the bottom of the melt zone. For example, it is observed that keyhole at position 2 is 7.5% deeper than the keyhole at position 1; thus, a spike is more likely to be formed under position 2, as shown in Fig. 15(b).

5.3 Analysis of Melt Pool Front Wall Angle

The melt pool front wall angle could also affect keyhole formation. Figure 16(a) shows the schematical plot of the transition process from a shallow melt pool to a keyhole. The three cases have the same laser power, but with different laser speed, e.g., $V_3 < V_2 < V_1$. When the laser travels at a high speed V_1, the melt pool has a shallow recession due to the Marangoni effect and the applied laser beam will get reflected upward. Decreasing the laser speed results in a material evaporation effect and the recoil pressure helps to create a deeper recession. At laser speed V_2, the melt pool front wall angle can cause the laser ray to be reflected horizontally. Strong evaporation effect will take place and cause significant recoil pressure if there is any further reduction in laser speed. At laser speed V_3, the melt pool is further recessed and the laser ray is
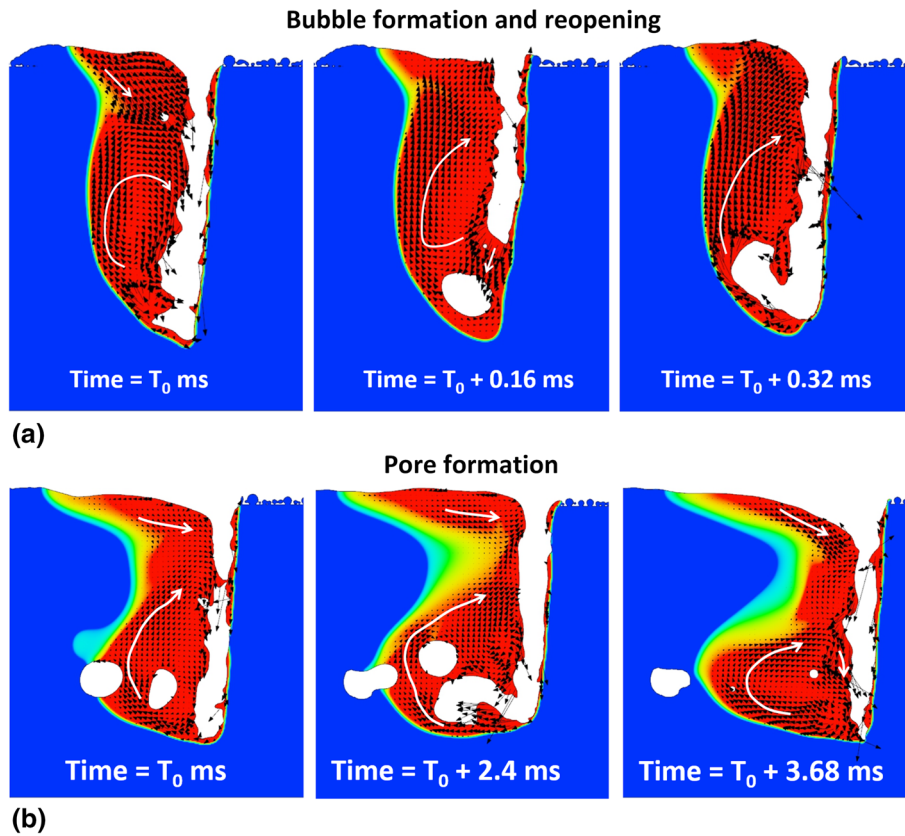
Bubble formation and reopening

Time = T$_0$ ms   Time = T$_0$ + 0.16 ms   Time = T$_0$ + 0.32 ms

(a)

Pore formation

Time = T$_0$ ms   Time = T$_0$ + 2.4 ms   Time = T$_0$ + 3.68 ms

(b)

Fig. 14 Keyhole dynamics for bubble and pore formation: (a) Bubble formation and reopening; (b) Pore formation
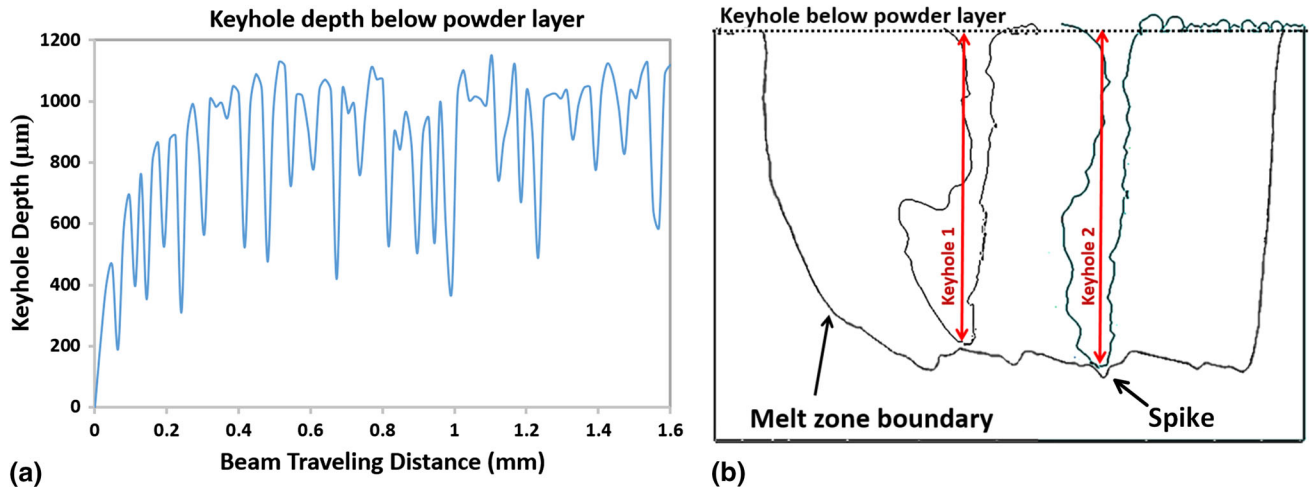

(a)

(b)

Fig. 15 Fluctuation of keyhole depth (below powder layer): (a) Keyhole depth (below powder layer) against beam traveling distance; (b) Development of spikes

reflected toward the bottom of the melt region, increasing the overall absorption rate inside the open recession and leading to a keyhole. The inclusion of a laser multi-reflection model (ray tracing) in the keyhole is the key to capture this phenomenon. It can be seen that the melt pool front wall angle increases along with the increase in laser line energy density [defined as laser power/speed (Ref 7)], as shown in Fig. 16(b). A nearly vertical

keyhole can be formed if the laser line energy density is very high, e.g., a front wall angle of 86° for 3.5 J/mm case.

5.4 Process Parameters Effect on Pore Generation

The scanning speed effect on keyhole and porosity formation is summarized in Fig. 17. With the same laser power of
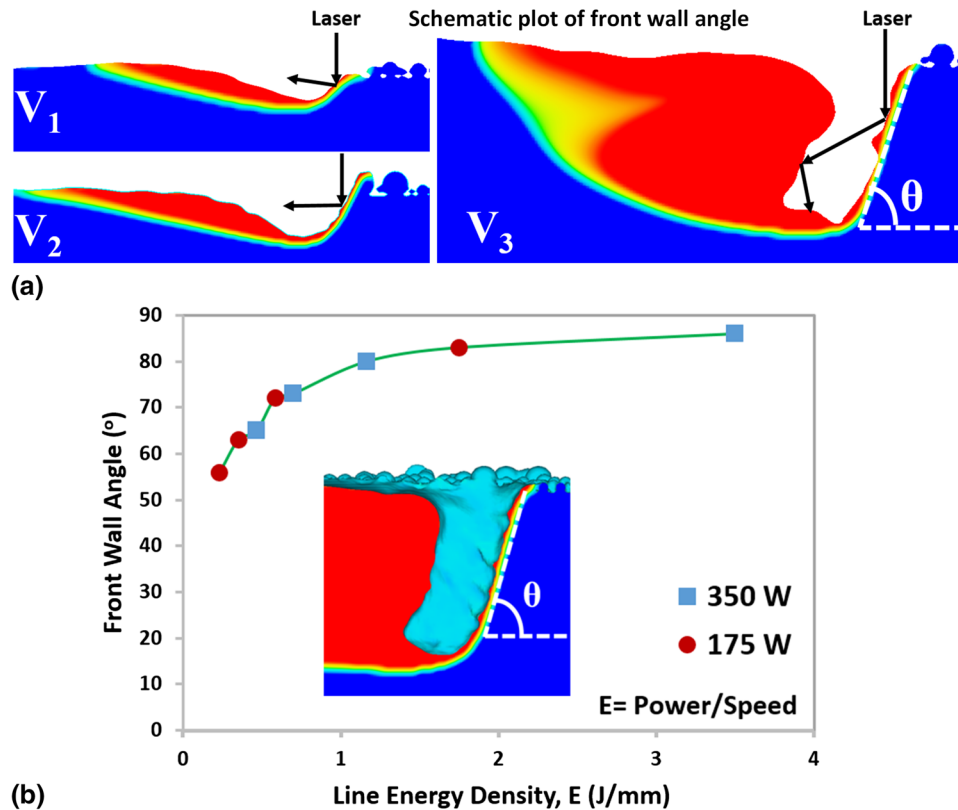
Fig. 16 Melt pool front wall at different laser powers: (a) Schematic plot of melt pool front wall angle and keyhole formation; (b) Front wall angle vs. laser line energy density

350 W, decreasing the laser scanning speed increases the intensity of the keyhole depth fluctuation, as shown in Fig. 17(a). It can be seen that the keyhole depth for the scanning speed of 750 mm/s has very small change along the scanning track, while the keyhole depth for 100 mm/s has intense variation along the melt track, e.g., the collapse of unstable keyhole could cause a keyhole depth change of over 400 μm at some locations, whereas the maximum keyhole depth can reach up to ca. 1000 μm. The unstable keyhole formation is caused by the interactions between strong melt pool flow that tends to close the keyhole and evaporation-induced recoil pressure that tends to reopen the enclosed bubble under the smaller keyhole. Figure 17(b) shows the maximum size of formed pores is increased with decreasing scanning speed. It can be explained that smaller scanning speed causes larger fluctuations of the keyhole depth, thus leading to formation of bigger sized gas bubbles in the melt pool which may finally be captured by the solidification front and turn into pore defects. The pore shape may not be spherical due to complex melt pool dynamics, as shown in Fig. 17(c).

Figure 18 compares the keyhole and pore characteristics generated by different laser powers. It is seen that higher laser power can lead to the generation of pore defect and larger pore size when subjecting to the same laser speed, as shown in

Fig. 18(a). Figure 18(b) shows that larger keyhole depth variation is observed for the 350 W laser power case. In addition, a larger variation of spikes (the variation range is marked using dotted lines) at the melt pool bottom is shown for the larger laser power case, e.g., the spike variation of high laser power case (H_{high}) is 39% bigger than that of low power case (H_{low}), as shown in Fig. 18(c).

6. Conclusion

In this study, a novel powder-scale multi-physics CFD model was applied to understand the physics of keyhole stability and pore generation in the L-PBF process. With the consideration of experimental powder particle size distribution, the DEM model was used to create one newly deposited powder layer upon a solid substrate. The geometrical information of the DEM simulated powder layer was imported to the CFD model for the melt pool dynamics simulation. Complex process physics, such as surface tension force, evaporation pressure and laser multi-reflection in the keyhole, were included in the thermo-fluid model. The major findings are summarized below:
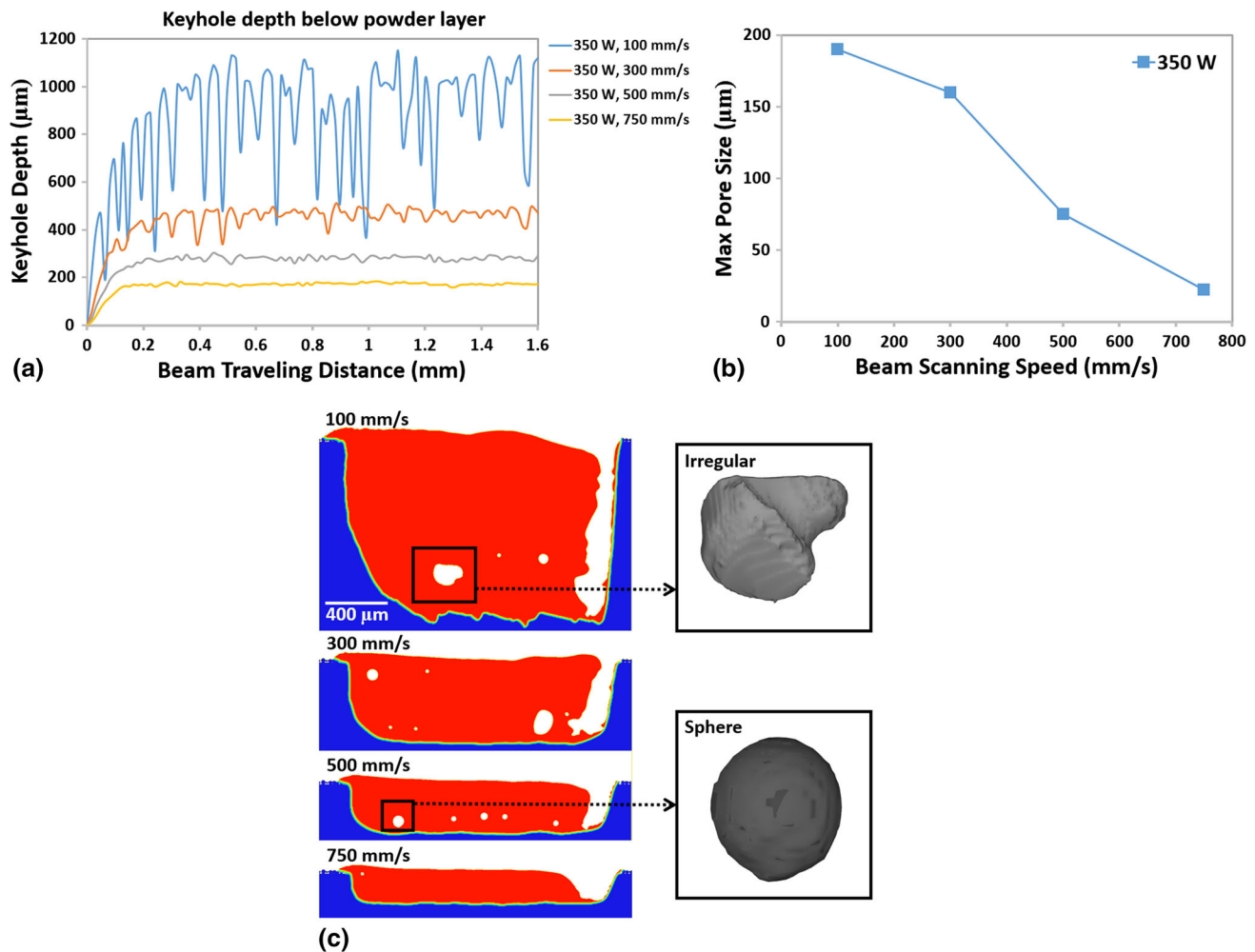
Fig. 17 Pore characteristics at different laser scanning speeds: (a) Summary of keyhole depth variation along scanning track; (b) Pore size and laser scanning speed; (c) Simulated irregular and spherical pore shapes

(1) The used model has been validated against experimentally measured melt pool dimensions coming from polished cross-sectional cuts. For the tested process parameters, the prediction error ranges from 1.3 to 10.6% for melt pool width while it ranges from 1.4 to 15.9% for depth.

(2) The collapse of unstable keyholes leads to the generation of bubbles in the melt pool and a pore is formed if a bubble is captured by the solidification front. The simulated pores in a scanning track are qualitatively comparable to CT measured pores at a laser power of 350 W and laser speed of 100 mm/s.

(3) The keyhole formation may be related to the melt pool front wall angle. A nearly linear relationship between melt pool front wall angle and laser line energy density is found from simulated results, e.g., front wall angle increases with the increase in line energy density.

(4) The formation of pores is observed at high laser energy density condition, e.g., low laser speed or high laser power. Under the same power, a smaller laser speed can result in a larger keyhole depth variation and lead to larger sized pores. Additionally, pores are more likely to be generated at larger laser power. Finally, a larger spike variation at the melt pool bottom can be observed for a smaller laser speed or larger power.
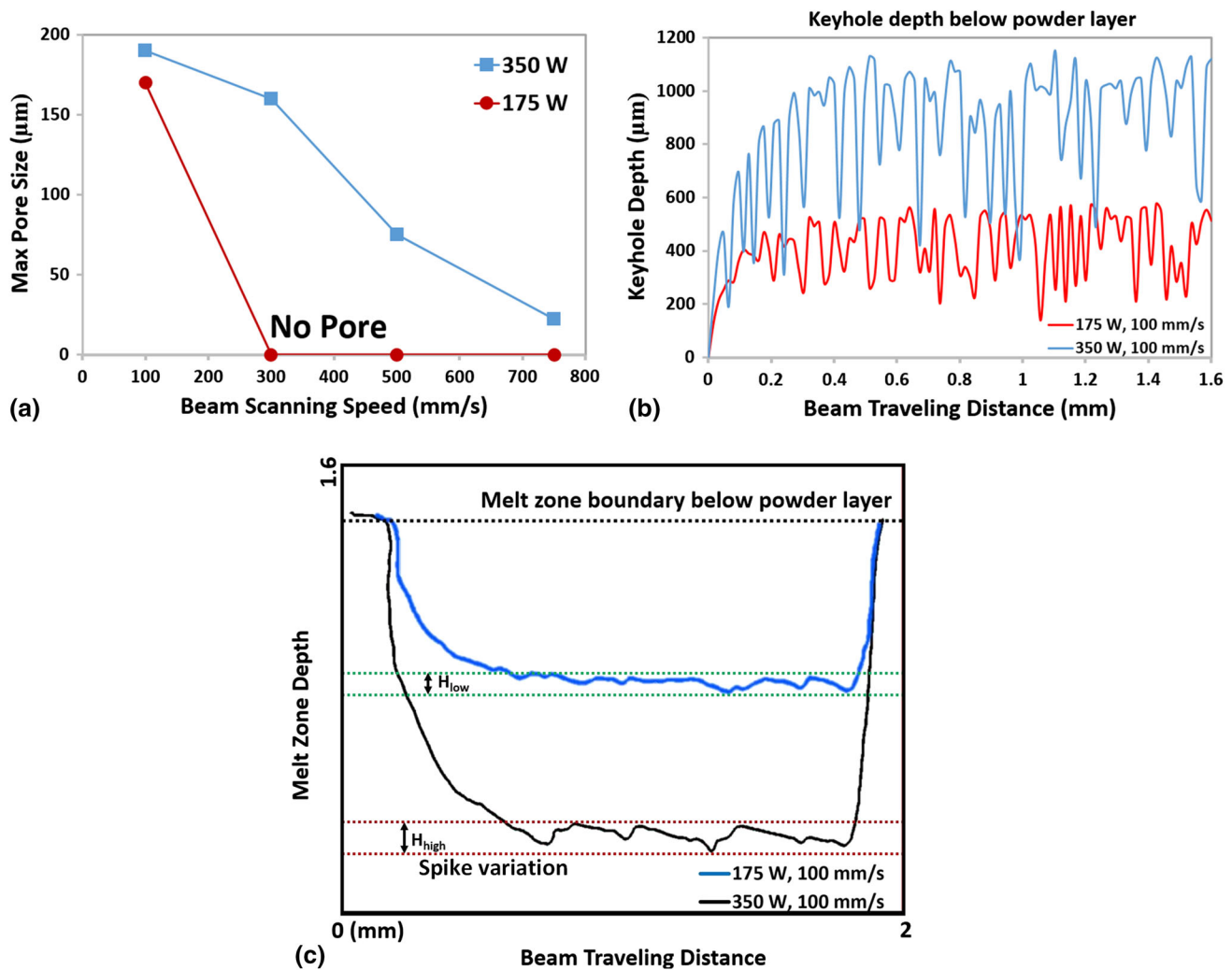
Fig. 18 Pore and melt zone characteristics at different laser powers: (a) Pore size and laser power; (b) Variation of keyhole depth at different laser powers; (c) Variation of melt zone spikes at different laser powers

References

1. S. Leuders, M. Thöne, A. Riemer, T. Niendorf, T. Tröster, H.A. Richard, and H.J. Maier, On the Mechanical Behaviour of Titanium Alloy TiAl6V4 Manufactured by Selective Laser Melting: Fatigue Resistance and Crack Growth Performance, *Int. J. Fatigue*, 2013, **48**, p 300–307
2. N.T. Aboulkhair, N.M. Everitt, I. Ashcroft, and C. Tuck, Reducing Porosity in AlSi10 Mg Parts Processed by Selective Laser Melting, *Additive Manufacturing*, 2014, **1**, p 77–86
3. H. Gong, H. Gu, K. Zeng, J.J.S. Dilip, D. Pal, B. Stucker, D. Christiansen, J. Beuth, and J.J.Lewandowski, Melt pool characterization for selective laser melting of Ti-6Al-4V pre-alloyed powder. In *25th Annual International Solid Freeform Fabrication Symposium—An Additive Manufacturing Conference,* Austin, TX, USA, August 4-6, 2014, pp. 256–267
4. S. Siddique, M. Imran, M. Rauer, M. Kaloudis, E. Wycisk, C. Emmelmann, and F. Walther, Computed Tomography for Characterization of Fatigue Performance of Selective Laser Melted Parts, *Mater. Des.*, 2015, **83**, p 661–669
5. X. Cai, A.A. Malcolm, B.S. Wong, and Z. Fan, Measurement and Characterization of Porosity in Aluminium Selective Laser Melting Parts Using X-ray CT, *Virt. Phys. Prototyp.*, 2015, **10**(4), p 195–206
6. S. Shrestha, T. Starr, and K. Chou, Individual and Coupled Contributions of Laser Power and Scanning Speed Towards Process-Induced Porosity in Selective Laser Melting. In *29th Annual International Solid Freeform Fabrication Symposium – An Additive Manufacturing Conference,* Austin, TX, USA, August 13–15, 2018, pp. 1400–1409
7. C.L.A. Leung, S. Marussi, R.C. Atwood, M. Towrie, P.J. Withers, and P.D. Lee, In Situ X-Ray Imaging of Defect and Molten Pool Dynamics in Laser Additive Manufacturing, *Nat. Commun.*, 2018, **9**(1), p 1355
8. R. Cunningham, C. Zhao, N. Parab, C. Kantzos, J. Pauza, K. Fezzaa, T. Sun, and A.D. Rollett, Keyhole Threshold and Morphology in Laser Melting Revealed by Ultrahigh-Speed X-Ray Imaging, *Science*, 2019, **363**(6429), p 849–852
9. S. Shrestha, K. Chou, Computational Analysis of Thermo-Fluid Dynamics with Metallic Powder in SLM. In *TMS Annual Meeting and Exhibition*, pp. 85–95. Springer, Cham, 2018
10. M. Xia, G. Dongdong, Yu Guanqun, D. Dai, H. Chen, and Q. Shi, Porosity Evolution and Its Thermodynamic Mechanism of Randomly Packed Powder-Bed During Selective Laser Melting of Inconel 718 Alloy, *Int. J. Mach. Tools Manuf*, 2017, **116**, p 96–106

11. W. Yan, W. Ge, Ya Qian, S. Lin, B. Zhou, W.K. Liu, F. Lin, and G.J. Wagner, Multi-physics Modeling of Single/Multiple-Track Defect Mechanisms in Electron Beam Selective Melting, *Acta Mater.*, 2017, **134**, p 324–333

12. J.L. Tan, C. Tang, and C.H. Wong, A Computational Study on Porosity Evolution in Parts Produced by Selective Laser Melting, *Metall. Mater. Trans. A*, 2018, **49**(8), p 3663–3673

13. Y.S. Lee and W. Zhang, Modeling of Heat Transfer, Fluid Flow and Solidification Microstructure of Nickel-Base Superalloy Fabricated by Laser Powder Bed Fusion, *Addit. Manuf.*, 2016, **12**, p 178–188

14. B. Cheng, X. Li, C. Tuffile, A. Ilin, H. Willeck, and U. Hartel, Multi-physics modeling of single track scanning in selective laser melting: powder compaction effect. In *29th Annual International Solid Freeform Fabrication Symposium—An Additive Manufacturing Conference,* Austin, TX, USA, August 13–15, 2018, pp. 1887–1902

15. W. Yu-Che, C.-H. San, C.-H. Chang, H.-J. Lin, R. Marwan, S. Baba, and W.-S. Hwang, Numerical Modeling of Melt-Pool Behavior in Selective Laser Melting with Random Powder Distribution and Experimental Validation, *J. Mater. Process. Technol.*, 2018, **254**, p 72–78

16. J.-H. Cho and S.-J. Na, Implementation of real-time multiple reflection and Fresnel absorption of laser beam in keyhole, *J. Phys. D Appl. Phys.*, 2006, **39**(24), p 5372

17. K.C. Mills, *Recommended Values of Thermo-physical Properties for Selected Commercial Alloys*, Woodhead Publishing, Cambridge, 2002, p 211–216

18. A. Masmoudi, R. Bolot, and C. Coddet, Investigation of the Laser–Powder–Atmosphere Interaction Zone During the Selective Laser Melting Process, *J. Mater. Process. Technol.*, 2015, **225**, p 122–132

19. W.E. King, A.T. Anderson, R.M. Ferencz, N.E. Hodge, C. Kamath, S.A. Khairallah, and A.M. Rubenchik, Laser Powder Bed Fusion Additive Manufacturing of Metals; Physics, Computational, and Materials Challenges, *Appl. Phys. Rev.*, 2015, **2**(4), p 041304

20. A.V. Gusarov and I. Smurov, Modeling the interaction of laser radiation with powder bed at selective laser melting, *Phys. Proc.*, 2010, **5**, p 381–394

21. I. Yadroitsev, P. Bertrand, and I. Smurov, Parametric Analysis of the Selective Laser Melting Process, *Appl. Surf. Sci.*, 2007, **253**(19), p 8064–8080